Tsunami inundation, sediment transport, and deposition process of tsunami deposits on coastal lowland inferred from the Tsunami Sand Transport Laboratory Experiment (TSTLE)

Article *in* Marine Geology · April 2018

DOI: 10.1016/j.margeo.2018.03.007

CITATIONS
14

READS
197

3 authors, including:

Takumi Yoshii
Central research institute of electric power industry, Japan
30 PUBLICATIONS **169** CITATIONS
SEE PROFILE

Masafumi Matsuyama
Central Research Institute of Electric Power Industry
83 PUBLICATIONS **617** CITATIONS
SEE PROFILE

Marine Geology 400 (2018) 107–118

Contents lists available at ScienceDirect

Marine Geology

journal homepage: www.elsevier.com/locate/margo

Tsunami inundation, sediment transport, and deposition process of tsunami deposits on coastal lowland inferred from the Tsunami Sand Transport Laboratory Experiment (TSTLE)

Takumi Yoshii[a,*], Shiro Tanaka[b], Masafumi Matsuyama[c]

[a] River and Coastal Environment Sector, Environmental Science Research Laboratory, Central Research Institute of Electric Power Industry, 1646 Abiko, Abiko, Chiba 270-1194, Japan
[b] Geosphere Science Sector, Civil Engineering Research Laboratory, Central Research Institute of Electric Power Industry, 1646 Abiko, Abiko, Chiba 270-1194, Japan
[c] Planning and Administrative Team, Nuclear Risk Research Center, Central Research Institute of Electric Power Industry, 1646 Abiko, Abiko, Chiba 270-1194, Japan

ARTICLE INFO

Keywords:
Tsunami deposit
Laboratory experiment
Sediment transport
Bed load
Inverse grading
Liquefaction

ABSTRACT

The processes of tsunami inundation, sediment transport, and deposition on coastal lowlands are investigated experimentally. We conducted large-scale experiments with land slopes of 0.00 and 0.01 and compared them with experiments conducted previously with a slope of 0.02. The ratio of marine-originated sediment in the inland deposits decreased as the land slope decreased, reflecting the strong inundation flow and weak return flow. The sediment concentration near the bed increased remarkably and supplied a greater quantity of coarse sand inland when the land slope decreased, indicating the strong influence of land slope on bed load. The extent of sandy deposits and the inundation limit nearly corresponded with the sloping topographies. However, the inundation flow reached much farther inland than the sandy deposits on the flat (i.e., level) topography. This was because the extent of sandy deposits was determined by the flow speed, which depended in turn on the wave speed, whereas the inundation limit was determined by the inland water mass, which depended in turn on the waveform. The floating load reached the inundation limit and formed very thin and sparse muddy deposits. Considering the uncertainty of the waveform and the difficulty of detecting muddy deposits, it is more feasible to estimate the wave speed from the extent of sandy deposits. The spatial distributions of sandy deposits for various waves, land slopes, and topographies were characterized by the nondimensional area density and inundation distance. This result suggested the possibility of quantitative comparison among field investigations of tsunami deposits under various conditions. The formation of an inverse grading layer, experimentally observed in a wide range of inland deposits, was attributed to kinetic sieving. The bed load under slow deposition was speculated to thicken the inverse grading layer by reworking the coarse sand. Additionally, the sediment behind dunes became liquefied and showed shear deformation during the erosion. The shear deformation of liquefied sediment below the erosional surface might leave sedimentary characteristics specific to earthquake tsunamis.

1. Introduction

Tsunamis cause extensive, multiple, and long-term disasters. Because coastal cities and their social infrastructure are vulnerable to flooding, the incursion of a tsunami has a catastrophic effect on the livelihood and economy of coastal regions. Furthermore, because a tsunami travels far from its source region without consuming much energy, it can also affect distant locations. Moreover, if a tsunami damages vitally important facilities, such as a nuclear power plant, the extent of the disaster-affected area can expand to the global scale (International Atomic Energy Agency, 2015). The relatively low frequency of megatsunamis poses a scientific challenge to preparing for possible future tsunamis. Information about the scale and recurrence period inferred from palaeotsunami deposits is indispensable for assessing previously unexperienced tsunamis and their sources.

The sedimentary characteristics of tsunami deposits have the potential to be used to reconstruct the hydraulic parameters of the tsunamis that caused the deposits. Recent studies have attempted to develop techniques for estimating the scale of tsunamis from sedimentary characteristics such as landward thinning and fining and normal grading, which are commonly observed in tsunami deposits (e.g., Peters and Jaffe, 2010b; Goff et al., 2010). The simplest approach to reconstructing the scale of a tsunami is to estimate its inundation distance (or height) from the extent of its deposits. Coupled with numerical

* Corresponding author.
E-mail address: takumi@criepi.denken.or.jp (T. Yoshii).

https://doi.org/10.1016/j.margeo.2018.03.007
Received 25 September 2017; Received in revised form 14 March 2018; Accepted 21 March 2018
Available online 04 April 2018

simulation, this technique has helped greatly to reveal the scale of undiscovered tsunamis and crustal movements (e.g., Nanayama et al., 2003; Satake et al., 2008; Sawai et al., 2012), although the difference between the inundation distance and the extent of deposits remains controversial (e.g., Shi et al., 1995; Gelfenbaum and Jaffe, 2003; Goto et al., 2011; Abe et al., 2012). Another approach is to estimate the inundation depth and velocity from the maximum extent of grains based on the relationship between the advection distance and the settling velocity of sand (Moore et al., 2007; Smith et al., 2007). Soulsby et al. (2007) offered a theoretical explanation of the hydrodynamic background of landward fining and grading of deposits by introducing a time-dependent water depth into this kind of conceptual model and calculated the maximum inundation height from the extent of sand. Jaffe and Gelfenbuam (2007) developed an inversion technique for the flow velocity based on the vertical distribution of suspended sediment; this technique exploits the grain size distribution of the tsunami deposits. More-recent approaches have combined the aforementioned techniques and succeeded in calculating both the flow depth and velocity from the distribution and grain size of deposits (e.g., Tang and Weiss, 2015; Naruse and Abe, 2017; Wang et al., 2018; Tang et al., 2018).

Although these inverse analyses provide useful information about palaeotsunamis (Witter et al., 2012; Spiske et al., 2013), the applicability of these inversion models is limited by simplifications in hydrodynamic processes and topographic conditions (e.g., Pritchard and Dickinson, 2008; Apotsos et al., 2011; Jaffe et al., 2016). Some sedimentary structures occasionally observed in deposits, such as cross-laminae (e.g., Nanayama, 2008), current ripple lamination (Naruse et al., 2010), and imbrication and orientation of grains (e.g., Takashimizu et al., 2012; Kain et al., 2014; Falvard and Paris, 2017) have been used to infer the flow direction. However, the other characteristics such as inverse grading are yet to be linked to the hydraulic parameters of tsunamis.

To realize the full potential of tsunami deposits for understanding tsunamis and to improve the accuracy of inversion models, the forward process from wave propagation to the formation of deposits (including entrainment of bed materials, sediment transport, and deposition) must be elucidated. Tsunami inundation and sediment transport, which form the sedimentary characteristics of deposits, are characterized mainly by the following features. 1) Tsunamis inundate uphill against gravity, unlike the usual flow of water. 2) Sediment supply is limited to that from the offshore and nearshore regions, and deposition dominates on land. 3) The inundation flow is fast and the sediment concentration can be very dense. 4) The inundated water becomes stagnant before it returns to the sea, thereby allowing suspended sediment to settle. 5) The return flow can erode the deposited sediment and carry it out to sea. 6) These phenomena can be repeated several times if there is a train of waves. These phenomena are undoubtedly responsive to geographical, geological, and hydrodynamical conditions. However, lack of field data (especially on hydraulic parameters) and considerable local variation of tsunami deposits (probably reflecting microtopography (e.g., Nishimura and Miyaji, 1995) and vegetation (e.g., Gelfenbaum et al., 2007)) in the field make it difficult to ascertain the relationship between the surrounding environment and the resulting deposits.

In a previous study, we succeeded in reproducing tsunami deposits on gently sloping topography ($\beta = 0.02$) in the Tsunami Sand Transport Laboratory Experiment (TSTLE) (Yoshii et al., 2017). Because of their scaling, traditional small-scale experiments are constrained to focus on local sediment transport (e.g., Takahashi et al., 2000; Yoshii et al., 2009) and deposits (e.g., Yamaguchi and Sekiguchi, 2015; Johnson et al., 2016). By contrast, this large-scale experiment (i.e., TSTLE) enabled us to reproduce tsunami inundation and sediment transport on a topography ranging from offshore to inland with a hydraulically reasonable scale. A large incident wave allowed the reproduction of strong inland and return flows (up to 3.5 m/s) and dense sediment transport (up to 5%). The resulting deposits showed landward and seaward thinning and fining and consisted of subunits with normal and inverse grading, which were commonly observed in the deposits in the field. TSTLE enables us to reveal the overall processes of tsunami propagation (e.g., shoaling, breaking, inundation, and backwash), sediment transport (e.g., erosion, suspension, deposition, and reworking), and deposits (e.g., thickness, grain size, mineral composition, and sedimentary structures). In particular, TSTLE provides a way to assess the dependence of tsunami deposits on parameters such as wave scale, land slope, and grain size because it offers better parametric control than is possible in field investigations.

This paper presents the results of experiments conducted as part of the TSTLE project that had topography similar to a coastal lowland with an aeolian dune, which is where tsunami deposits have been investigated most frequently. This study focuses on two major objectives. The primary objective is to clarify tsunami inundation, bed erosion, sediment transport, and the resulting lowland deposits by comparing experiments with different land slopes and wave heights. The secondary objective is to investigate the depositional process of an inverse grading layer, which remains poorly understood from previous experiments.

2. Methods

2.1. Laboratory experiments

To maintain data compatibility with previous experiments, the laboratory experiments, sampling, and analysis methods used here were the same as those in Yoshii et al. (2017). The flume channel was 0.6 m wide and 90 m long, with a seabed slope of 0.02 and a land slope (β) of 0.01 or 0.00 (Fig. 1). The subsequent waves, return flow, and overflow were controlled by three gates located at $x = 0.0$, 40.7, and 90.0 m. Silica-dominant sand covered the floor for $x = 0$–50 m, and a sand dune (height: 0.2 m; width of crest: 0.2 m; total width: 0.8 m) was located at $x = 40.4$ –41.2 m. The bed sand, which contained iron sand (D50: ≈0.12 mm), had a bimodal grain-size distribution with a sharp peak at 0.2 mm (58%) and a small peak at 1–2 mm (12%). The bed materials were mainly SiO_2 (73.8%), Al_2O_3 (10.9%), and Fe_2O_3 (7.3%).

We examined seven experimental cases (Table 1). The height of the bore waves in C6 and C7 was adjusted to avoid overflowing the channel (Fig. 2). Absorbing waves were made in C11–13 to reduce the subsequent waves and return the water level to the original level. Sediment traps made from a plankton net ($\phi = 95$ μ m) were used to measure the vertical distribution of sediment transport at $x = 51$ m in C10. The erosion and deposition processes were recorded using normal-speed (100 fps, 1920 × 1080 pixels) and high-speed (500 fps, 640 × 480 pixels) cameras through a transparent wall at $x = 39$–45 m. We obtained the deposits at $x = 20$–89.75 m and measured their chemical composition, the weight fraction of grains equal to or larger than 1 mm (D_{vcs}), and the median diameter of grains smaller than 1 mm ($D50$).

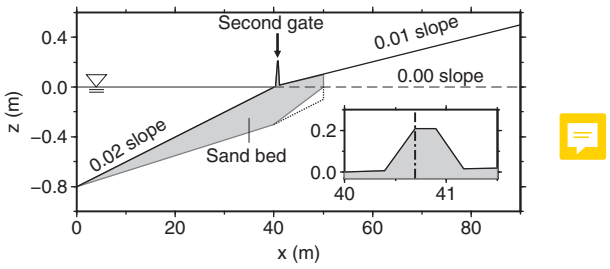

Fig. 1. Sectional view of the movable-bed channel. The gray colored area indicates the sand bed. The broken and dotted lines show the surface and bottom, respectively, of the sand bed in the 0.00 slope experiments. The inset shows a magnified portion of the sectional view. The chained line indicates the location of the second gate.

Table 1
Conditions for experimental cases. The case name follows previous experiments with a slope of 0.02 (C1–C5) reported in Yoshii et al. (2017). $MTH_{0.5}$ indicates the maximum water level of the progressing wave at $x = 0.5$ m, and MWL_{40} and V_{max} indicate the maximum water level and the maximum horizontal velocity at the shoreline, respectively.

Case	Slope	Waveform	Dune	2nd gate	Trap	$MTH_{0.5}$ (m)	MWL_{40} (m)	V_{max} (m/s)
C6	0.01	Bore	×	×	×	0.30	0.29	2.6
C7	0.01	Bore	✓	×	×	0.36	0.49	2.5
C8	0.01	Peaked	✓	×	×	0.73	0.68	3.0
C9	0.01	Peaked	✓	✓	×	0.72	0.67	3.8
C10	0.01	Peaked	✓	×	✓	0.72	0.65	3.4
C11	0.00	Bore	✓	×	×	0.17	0.31	2.1
C12	0.00	Bore	✓	×	×	0.38	0.51	2.6
C13	0.00	Peaked	✓	×	×	0.74	0.66	3.4

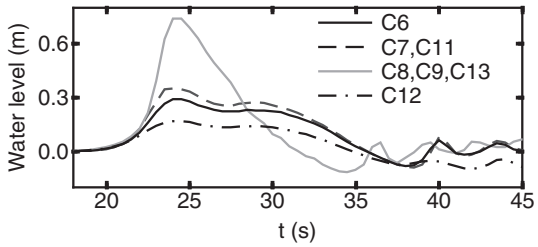

Fig. 2. Progressing waves observed at $x = 0.5$ m. The time axis (t) is defined as the elapsed time from the start of wave generation.

2.2. Data analysis

To compare the results for various hydraulic and topographic conditions, we introduced nondimensional parameters. The nondimensional area density of deposits (A') is presented in the form

$$A' = A(w_g/V_0)^2/(\rho_s D50), \quad (1)$$

where A, w_g, V_0, and ρ_s indicate the area density of the deposits, the settling velocity (2.75 cm/s), the inundation speed at the shoreline, and the density of sediment (2.84 g/cm^3), respectively. The nondimensional term $(w_g/V_0)^2$ corrects for the effect of the magnitude of the tsunami on the amount of tsunami deposit, and the term $\rho_s D50$ corrects for the variation caused by the characteristics of the bed materials. Replacing the area density by the thickness of deposits (D) gives

$$A' = D(w_g/V_0)^2(1-\varepsilon)/D50, \quad (2)$$

where ε is the porosity of deposits.

The nondimensional inundation distance (L') is given by

$$L' = L/L_f, \quad (3)$$

where L is the distance from the shoreline and L_f is the maximum distance at which the flow speed is larger than the minimum speed for sediment movement (V_{min}) (hereinafter referred to as the flow distance). Because the maximum horizontal velocity occurs at the front of the inundation flow and the deceleration of the inundation flow is proportional to the component of gravity parallel to the slope, as experimentally confirmed by Yoshii et al. (2017), the maximum horizontal velocity (V) at any distance from the shoreline is given by

$$V = V_0 - g t_s \sin\theta, \quad (4)$$

where g is the acceleration due to gravity (9.8 m/s^2), t_s is the period from the beginning of inundation, and θ is the angle of the land slope ($\beta/\sqrt{1+\beta^2}$). By integrating Eq. (4), the flow distance is given by

$$L_f = (V_0^2 - V_{min}^2)/(2g\sin\theta). \quad (5)$$

Because we can assume $V_{min} \ll V_0$ for sandy deposits in the field, the flow distance is given here by

$$L_f \approx V_0^2/(2g\sin\theta). \quad (6)$$

3. Results

3.1. Inundation and return flows

The deceleration of the inundation flow decreased as the land slope became gentler (Fig. 3 (a)). The deceleration of the inundation flow caused by bore waves on the 0.02 and 0.01 slopes was consistent with that expected from the gravity effect, whereas that on the flat topography was consistent with that excepted on a slope of 0.006 (0.055 m/s^2). The deceleration of the peak wave was larger than that of the bore wave. The difference was constant at 0.07 m/s^2 regardless of land slope, indicating that the wave form influenced the deceleration of the inundation flow as already indicated in Yoshii et al. (2017).

The inundation flow in C11 reached farther than the flow distance. The deceleration of the inundation flow was consistent with that in C12 at $x < 74$ m and became appreciably smaller with distance at $x \geq 74$ m. The Shields number of the 0.2-mm-diameter sand decreased to less than the critical Shields number (0.07) at $x = 74$ m.

The maximum velocity of the return flow (V_r) also decreased as the land slope became gentler. The slope of V_r in the cross-shore direction showed no appreciable difference between bore and peak waves (Fig. 3 (b)). The slope was represented as the following equation by using the distance from the inundation limit (x_i):

$$V_r = 4.0 \cdot \beta \cdot x_i. \quad (7)$$

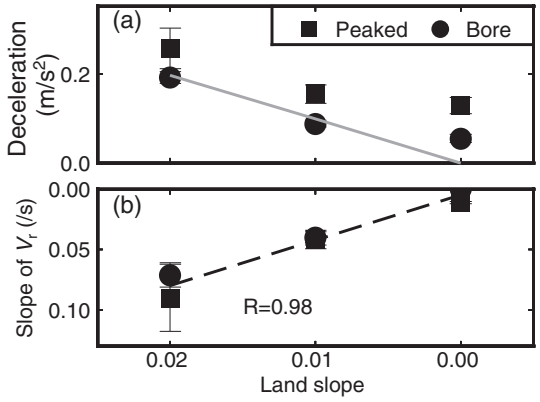

Fig. 3. (a) Deceleration of inundation flow and (b) slope of spatial distribution of maximum velocity of return flow (V_r). The gray solid line in (a) indicates the deceleration calculated from the effect of gravity. The dashed line in (b) indicates the regression line. The error bars indicate standard deviation.

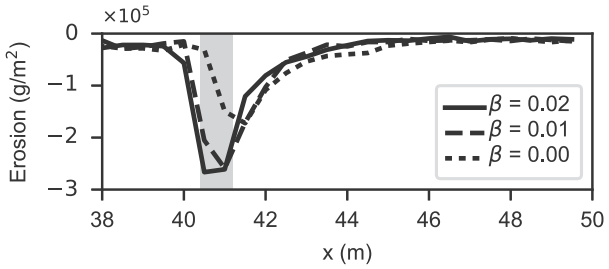

Fig. 4. Spatial distribution of erosion in the peak wave experiments. The gray area indicates the position at which the dune is located.

3.2. Topography change and deposits

3.2.1. Amount of erosion

The scour behind the dune expanded inland as the land slope became gentler, reflecting the stronger inundation flow (Fig. 4). As a result, the erosion behind the dune caused by the peak wave increased from 2.5×10^5 ($\beta = 0.02$) to 2.8×10^5 ($\beta = 0.01$) and 3.5×10^5 g/m ($\beta = 0.00$). The wave did not erode the dune completely in the experiments with flat topography, and the erosion of the dune was 42% (C11), 67% (C12), and 42% (C13). The offshore erosion for $\beta = 0.01$ decreased by 17–26% compared with $\beta = 0.02$, and the offshore erosion on the flat topography was estimated to be 73% of that for $\beta = 0.01$.

3.2.2. Amount of deposits

The total amount of deposits increased by 35% (no dune), 5% (bore wave with dune), and 4% (peak wave) as the land slope decreased from 0.02 to 0.01 (Fig. 5). In contrast, the amount decreased by 13% on the flat topography because the erosion of the dune decreased. As the land slope decreased, the ratio of inland deposits to total deposits increased. The proportion of inland deposits to total deposits on the topography without the dune increased from 20% ($\beta = 0.02$) to 47% ($\beta = 0.01$). In the experiments with the dune, the proportion increased from 42% to 78% (bore wave) and from 43% to 70% (peak wave) when the land slope decreased from 0.02 to 0.00.

3.2.3. Source of deposits

As the land slope became gentler, the proportions of inland- and nearshore-originated sediment in the offshore deposits decreased and that of the inland-originated sediment in the inland deposits increased (Fig. 6). Because the increased erosion behind the dune increased the inland-originated sediment in the inland deposits, the proportion of offshore sediment in the inland deposits decreased from 30% ($\beta = 0.02$) to 14% ($\beta = 0.02$). Meanwhile, the inland and dune sediment in the offshore deposits considerably decreased when the topography became flat because there was no return flow. The proportions for $\beta = 0.02$

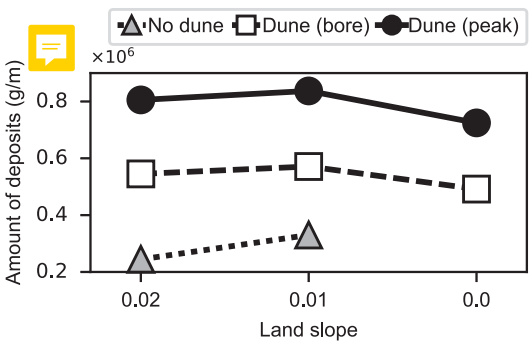

Fig. 5. Total amount of deposits. The amount includes the sediment that overflowed at the end of the channel (1.0×10^3 g/m in C8, 9.4×10^3 g/m in C12, and 4.8×10^4 g/m in C13).

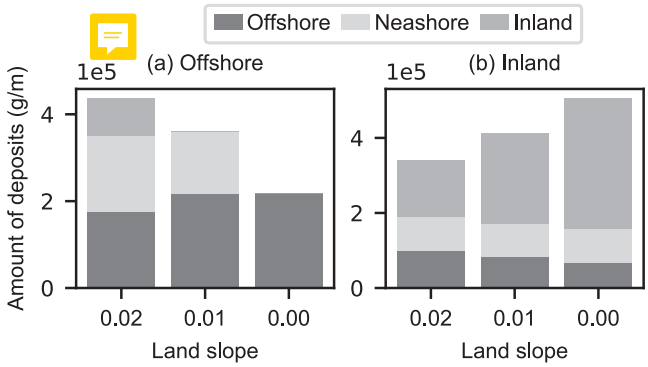

Fig. 6. Source of (a) offshore deposits and (b) inland deposits in the peak wave experiments. The offshore, nearshore, and inland areas correspond to x = 0–40.0, 40.0–41.2, and 41.2–90 m (65 m at $\beta = 0.02$), respectively. The overflowed sediment is considered in the inland deposits.

were slightly different from our previous report (Yoshii et al., 2017) because the erosion of the dune was obtained from C13 and not by comparing the experiments with and without operation of the second gate.

3.2.4. Spatial distribution of inland deposits

The area density of deposits showed that landward thinning and its rate of decrease diminished as the land slope became gentler. However, the decreasing trend for different slopes was similar in the nondimensional scale, although there was considerable variation (Fig. 7 (a)). According to the regression line, the nondimensional area density decreased to 0.1% of that at the shoreline when L' reached 1.0, and the density decreased rapidly to < 0.002% at $L' = 1.5$. The grain-size distribution showed landward fining especially at $L' > 0.9$ (Fig. 7 (b)). The chemical composition of deposits also showed rapid change at $L' > 0.9$ (Fig. 7 (c),(d)).

3.2.5. Vertical distributions of grain size and chemical composition of deposits

The sedimentary structure of deposits formed in these experiments was similar to that on the 0.02 slope topography reported in Yoshii et al. (2017) (Fig. 8). The deposits obtained at x = 50.25–53.25 m showed inverse grading near the bottom and normal grading on the upper layer. The Fe_2O_3 content showed upward decrease and the Al_2O_3 content showed upward increase. However, the very coarse sand became concentrated near the surface on the flat topography, whereas the peak of D_{vcs} appeared in the middle of the deposits on the sloping topographies. While the Fe_2O_3 content increased slightly at the surface in some deposits on the 0.02 and 0.01 slopes, that of the deposits on the flat topography did not increase at the surface.

3.3. Sediment transport

3.3.1. Sediment concentration

The time-averaged concentration decreased in the landward direction, and there was little difference in experimental conditions except near the dune (Fig. 7 (e)). The concentration on the topography with the dune showed rapid decrease behind the dune compared with that on the topography without the dune, as already indicated by Yoshii et al. (2017). The concentration at $L' > 0.2$ decreased at an exponential rate. The concentration in C11 was extremely high behind the dune (14%) and decreased rapidly to 0.7% at x = 54 m.

The ratio of deposit thickness to maximum inundation depth (hereinafter referred to as the pseudo-concentration) showed landward increase (Fig. 7 (f)). The considerable deposition at the scour behind the dune resulted in the high pseudo-concentration at $L' \leq 0.3$. Except for these large concentrations behind the dune and at $L' > 0.9$, the pseudo-

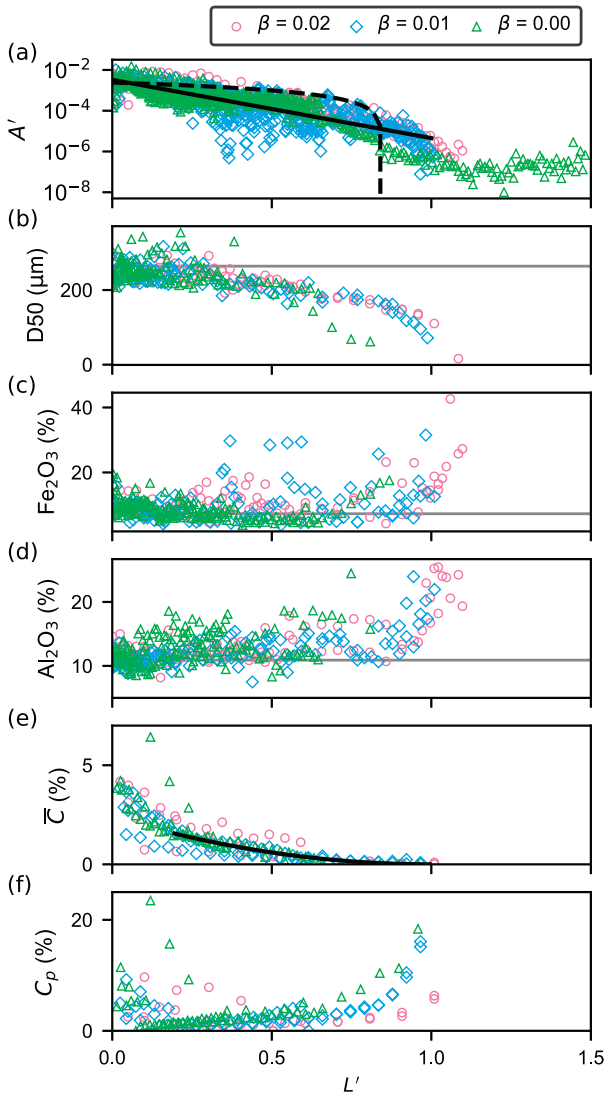

Fig. 7. Spatial distribution of (a) nondimensional area density of deposits, (b) D50, (c) Fe_2O_3 content, (d) Al_2O_3 content, (e) time-averaged concentration, and (f) pseudo concentration against the nondimensional inundation distance. The nondimensional area density (a) is presented as a semi-logarithmic graph. The solid and dashed lines in (a) indicate the regression lines of this experiment ($A' = 10^{-2.9L'-2.5}$, $R = -0.81$) and that on Sendai Plain ($D = -2.6 \times 10^{-5}L + 0.11$) reported in Goto et al. (2014), respectively. An equivalent slope of 0.006 was used for the land slope on the flat topography. The initial inundation speed (V_0) on Sendai Plain was estimated to be 11 m/s from Sugawara and Goto (2012) and the flow distance was estimated to be 5000 m. The horizontal lines in (b)–(d) indicate the values of the initial bed. The concentrations at $L' = 0.08$ in C11 (13.7% in (e) and 29.8% in (f)) are beyond the figures. The regression line in (e) is $\overline{C} = 2.4 \times (1 - L')^2$ ($R = 0.94$).

concentration ranged mainly from 0.8% to 5%; however, there were considerable differences among the experimental cases.

3.3.2. Vertical distribution of sediment transport

The vertical distributions of time-averaged concentration ($\overline{C}$), D_{vcs}, $D50$, and Fe_2O_3 content for $\beta = 0.01$ showed upward decrease, whereas the Al_2O_3 content showed upward increase (Fig. 9). These trends were consistent with those for $\beta = 0.02$. The $D50$ value for $\beta = 0.01$ was slightly larger than that for $\beta = 0.02$, probably reflecting the fact that the $D50$ value of the pre-experimental bed was slightly larger than that in the experiment with $\beta = 0.02$.

The remarkable difference between the experiments for $\beta = 0.02$ and 0.01 was that the concentration near the bottom for $\beta = 0.01$ was much higher than that for $\beta = 0.02$. This was because D_{vcs} and the amount of deposits at $x > 51$ m for $\beta = 0.01$ (4.8% and 1.8×10^5 g/m, respectively) were larger than those for $\beta = 0.02$ (3.3% and 1.3×10^5 g/m, respectively). To explain the D_{vcs} values at $x > 51$ m, the concentration near the bottom for $\beta = 0.01$ should be larger than that for $\beta = 0.02$. The total sediment in the inundation flow estimated by the trap was 119% of the deposits at $x > 51$ m, indicating that the concentration was overestimated slightly.

The D_{vcs} value and the amount of deposits at $x > 51$ m in C13 were 5.5% and 2.5×10^5 g/m, respectively, indicating that the inundation flow on the flat topography carried more coarse sand inland than it did on the sloping topography. Assuming that the vertical distribution for $\beta = 0.00$ was the same as that for $\beta = 0.01$, the concentration near the bottom in C13 was estimated to be up to 40%. Although this estimation explains the D_{vcs} values at $x > 51$ m, this estimated concentration overestimates the amount of sediment at $x > 51$ m by 140%.

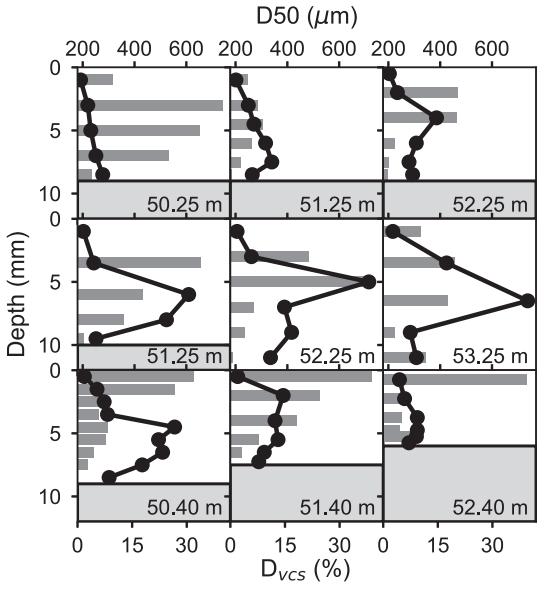

Fig. 8. Vertical distributions of D_{vcs} and D50 in the deposits on a land slope of (top) 0.02, (middle) 0.01, and (bottom) 0.00. The horizontal bars indicate D_{vcs}, and the black circles indicate D50. The horizontal lines indicate the bottom of the deposits. The sampling points are indicated in each figure.

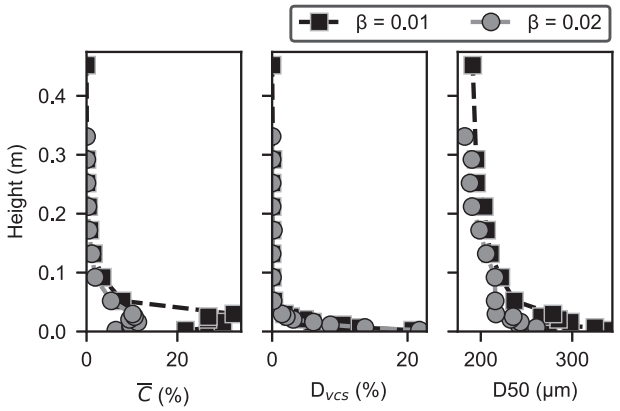

Fig. 9. Vertical distributions of time-averaged concentration ($\overline{C}$), D_{vcs}, and D50 in the inundation flow.

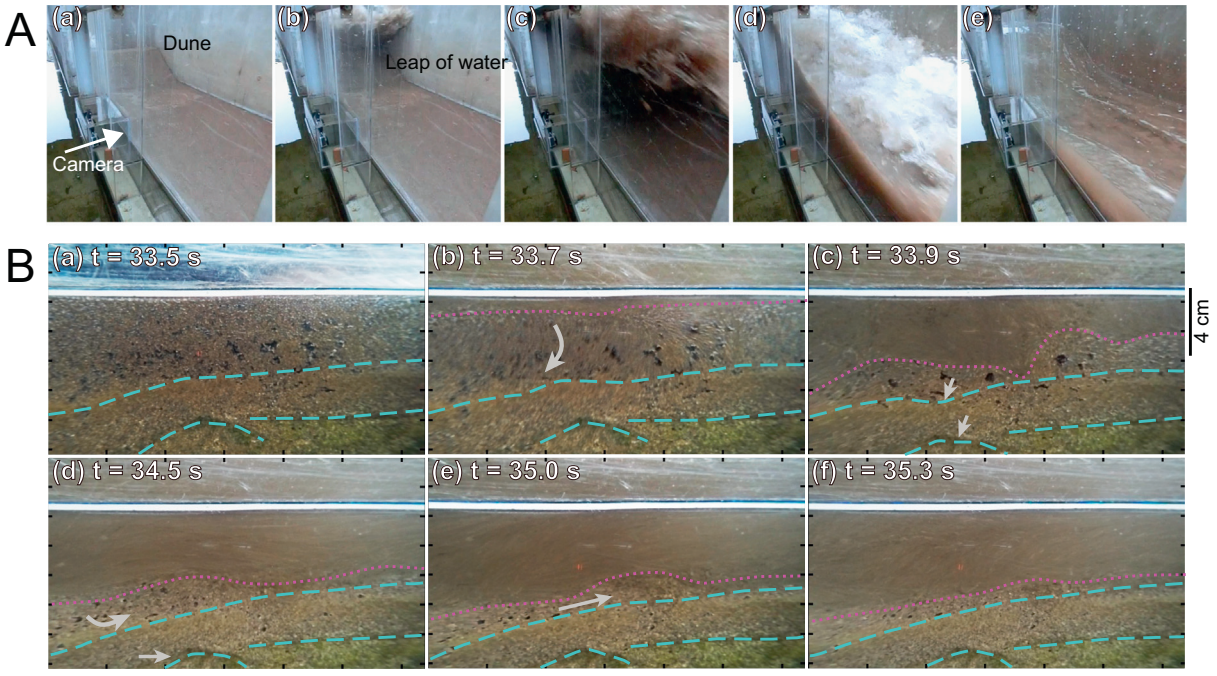

Fig. 10. (A) Inundation behind the dune and (B) liquefaction observed at $x = 41.5$ m in C8. The original surface located at the top of the white band and the reddish dotted lines indicate the bed surface at each time. The pattern of lateral stripes observed in the sediment and its transformation are indicated in blue broken lines. The video footage is available in Appendix A. (For interpretation of the references to color in this figure legend, the reader is referred to the web version of this article.)

3.4. Erosion and deposition processes

3.4.1. Consolidation and liquefaction behind the dune

We confirmed that consolidation and liquefaction occurred at $x = 41.5$ m in C8 from the video images (Fig. 10). Firstly, instantaneous compression occurred immediately upon wave arrival, reaching 5 cm below the surface (Fig. 10B(a)–(c)). The sediment 4 cm below the surface moved simultaneously, resulting in rapid and appreciable erosion. The sediment below the solid–liquid interface showed landward shear deformation caused by the flow (Fig. 10B(d) and (e)). As the flow became a stable landward flow, the disturbed interface became smooth (Fig. 10B(f)). The pressure caused by the collision of the overtopping water (Fig. 10A) was not appreciable where the liquefaction was observed ($x = 41.5$ m), whereas the impulsive pressure appeared at $x \geq 42.0$ m where the initial erosion was much less than that at $x = 41.5$ m. There was considerable variation in the maximum value of the impulsive pressure (5–116 g/cm^2).

Liquefaction was not observed in every experiment. The experiments with similar hydraulic parameters (C9 and C13) did not show similar phenomena. The erosion in C8 was almost the same as that in C9, indicating that liquefaction did not affect the erosion process.

3.4.2. Deposition process

The high-speed camera behind the dune ($x = 41.6$ m) observed the formation of deposits that comprised two subunits consisting of an iron-dominant bed layer, an inverse grading, and a normal grading (darker and lighter gray layers in Fig. 11A). The video images showed that the lower part of the deposits formed in approximately 0.2 s at the end of the landward flow. After this rapid and notable deposition, the suspended sediment became concentrated near the bed and accumulated gradually on the surface. As the surface of the pooled water in the scour behind the dune rose, the return flow began to plunge into this pooled water, causing strong vertical mixing. The upper part of the deposits began to form under this mixing and thickened as the return flow accelerated and brought more sediment. The rate of deposition of the upper part was gradual compared with that of the lower part.

The high-speed camera at $x = 44.4$ m revealed gradual accumulation of sediment during the landward flow (Fig. 11B). In contrast to the rapid deposition behind the dune, there was a bed load during the accumulation. The video recorded the deposition process of the lower subunit of the deposits, which comprised an iron-dominant bed layer, an inverse grading, and a normal grading. The sedimentary structure of these deposits was similar to that behind the dune. Coarse sand appeared in greater quantity in the upper part of the deposits than it did behind the dune.

4. Discussion

4.1. Hydraulic features

The deceleration (resp., acceleration) of the inundation (return) flow depended on the land slope, wave form, and bottom friction (Fig. 3(a)). Because the effect of gravity became less dominant as the slope became gentler, the bottom friction and waveform became dominant on the flat topography. Specifically, the effect of the waveform was at the same level as that of the bottom friction on the flat topography. We speculate that the stronger turbulence in the inundation flow of the peak wave caused larger energy loss (Yoshii et al., 2017). It would be important to evaluate the effect of the waveform when estimating the flow distance on the flat topography.

The physical meaning of the inundation limit on the flat topography differed from that on the sloping topography. The inundation limit corresponded nearly to the flow distance on the sloping topography, whereas the inundation limit reached farther than the flow distance on the flat topography. Because the flow distance is governed by the initial inundation speed (Eq. (5)), the inundation limit on the sloping topography reflected the inundation speed at the shoreline. Meanwhile, the inundation limit on the nearly flat topography reflected the inland water mass. The inundation beyond the flow distance on the flat topography was very slow because this flow was driven by the slope of the water surface. The importance of this classification on the interpretation of deposits is discussed in Section 4.6.

The effect of the waveform on the return flow is small, which allows estimating the maximum velocity of the return flow from the

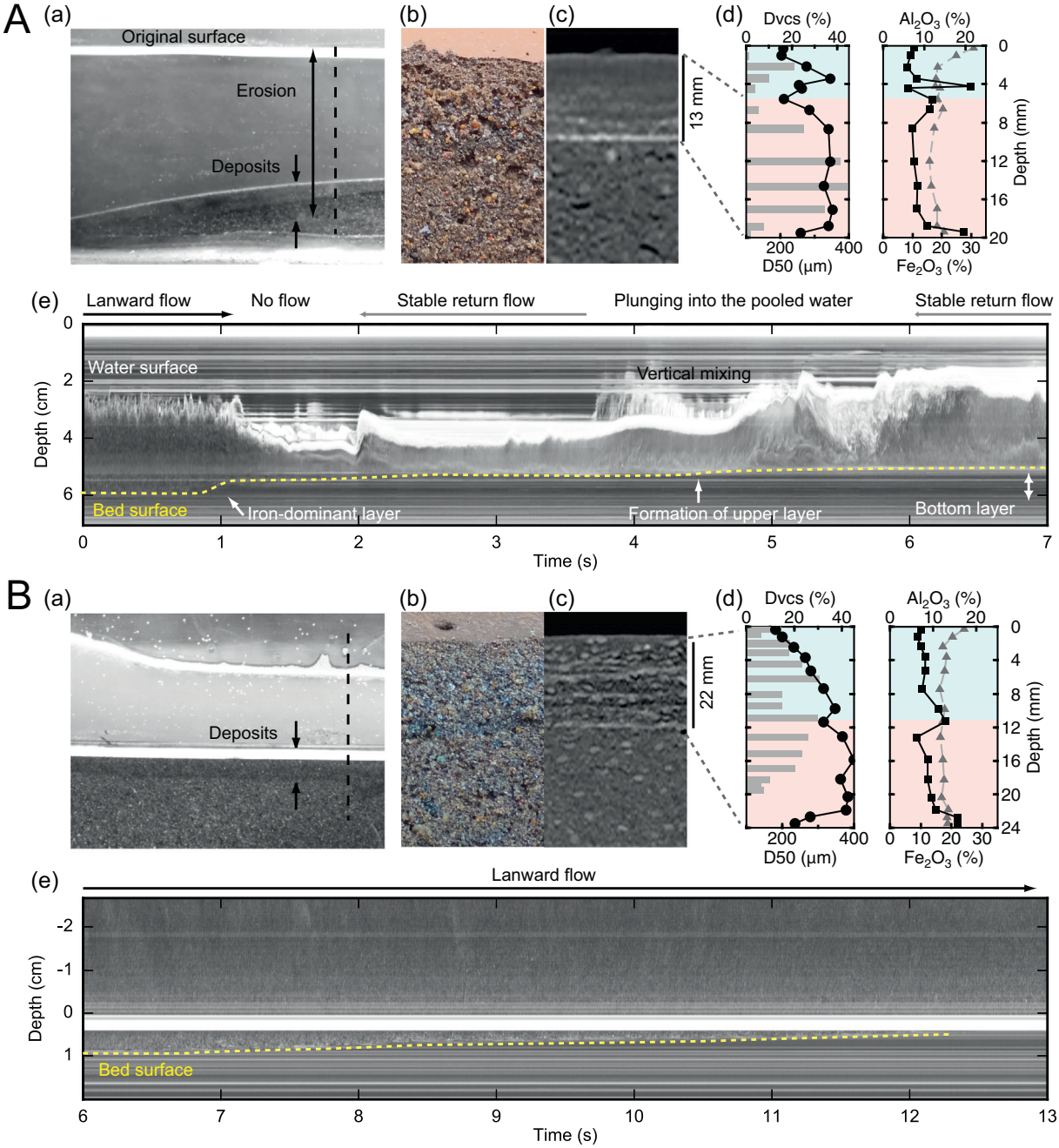

Fig. 11. Deposits and high-speed images at x = (A) 41.6 m and (B) 44.4 m in C13. (a) Post-experimental topography, (b) photograph, and (c) computed tomography image of the deposits, (d) grain size and chemical composition of the deposits, and (e) time-stack image of the recorded image. The broken line in (a) indicates the line used for the time-stack image. The circles, squares, triangles, and horizontal bars in (d) indicate $D50$, D_{vcs}, Fe_2O_3 content, and Al_2O_3 content, respectively. The horizontal stripe patterns in the time-stack images reflect stains or bubbles. The photograph and computed tomography images show deposits at x = 41.5 m in (A) and at x = 44.5 m (B). The grain size and chemical compositions show those of deposits at x = 42.0 m (A) and at x = 44.0 m (B). The original video footage is available in Appendix A.

inundation limit (Eq. (7)). Since the return flow becomes negligibly small in the most terrestrial region on the flat topography, and so it neither disturbs the accumulation of sediment nor causes re-suspension. However, the water plunging into the scouring behind the dune induced a return flow (see Fig. 11A and the video footage in supplementary data). Although this return flow appeared only near the dune, it can form deposits with two subunits even on the flat topography (Fig. 11A(d)). Considering that the water surface has a small slope after tsunami inundation on the flat topography, the local topography would be more important for interpreting the subsequent flow field compared to the sloping topography.

4.2. Sediment sources

The major sediment source of inland deposits on the topography with a nearshore dune was confirmed to be the nearshore region by field measurements (Szczuciński et al., 2012), numerical simulations (Sugawara and Goto, 2012), and laboratory experiments (Yoshii et al., 2017). This is because the superposition of the incident and reflected waves in front of the dune decreases the landward flow drastically (Sugawara and Goto, 2012; Yoshii et al., 2017). Our experiments revealed that the inland-originated sediment became more dominant in the inland deposits and the offshore deposits became poor in the inland

sediment as the land slope became gentler (Fig. 6). This feature was attributed not only to the weaker return flow but also to the stronger inundation flow. The stronger inundation flow increased the sediment supply from the scour behind the dune (Fig. 4), whereas the weaker return flow promoted the deposition of suspended sediment on the inland region.

These results indicate that deposits on a flat topography are more likely to lack marine-originated indicators (e.g., diatoms and shells) that help to identify tsunami deposits. However, considering that the increase of inland-originated sediment was not large compared with the total amount of inland deposits, its effect on identifying inland deposits would be limited. By contrast, because the sediment supply from inland and nearshore to the offshore regions disappears on flat topography, it would be more difficult to identify offshore deposits. Considering that the duration of the horizontal flow in the offshore region was short because of the superposition of waves and the offshore topography change was small, the sediment suspended by the incident wave would settle near its original location. The lack of mixing of sediment in the cross-shore direction can lead to deposits that have the same mineral composition as that of the original bed material. Therefore, we may need to develop identification criteria for offshore tsunami deposits based on sedimentary characteristics.

4.3. Generalization of sediment distribution and concentration

The hydraulic difference caused by the land slope affected the extent of tsunami deposits and distribution of area density; however, the spatial distribution of sedimentary characteristics was generalized by using the nondimensional inundation distance and area density. The time-averaged concentrations (except for those in the nearshore region) for various topographies and incident waves were also expressed as functions of the flow distance ($1 - L'$). These results suggested the possibility of separating the general phenomena from the site-specific phenomena caused by local topographic effects and hydraulic performance. Because it is difficult to investigate the effect of site-specific phenomena on ancient tsunami deposits, evaluating the general trend and variation would be important when interpreting ancient tsunami deposits.

The extent of sandy deposits corresponded to the flow distance ($L' = 1.0$), indicating that the flow distance would be a good indicator for classifying the dominant sediment-transport mechanism (Fig. 7 (a)) if deposits were made by one inundation and the topography is sufficiently uncomplicated to be treated as a uniformly sloping topography. The rapid change of grain size and chemical composition near the flow distance (Fig. 7 (b)–(d)) indicated that the dominant sediment-transport form changed from a suspended load to a muddy floating load (Yoshii et al., 2017). Because the floating load can be carried even by shallow and slow flow, the muddy sediment reached the inundation limit. It was impossible to generalize the range difference in the extent between sandy deposits and muddy deposits because the governing parameters were different; however, the extent of sandy deposits could be generalized by the flow distance.

The generalization of area density (deposit thickness) remains an issue because there was considerable difference in the nondimensional area density for different hydraulic and topographic conditions. Firstly, the generalization was not evaluated by the field measurements. The nondimensional area density of the field measurements on Sendai Plain (mostly for $\beta < 0.001$) (Goto et al., 2014) was consistent with our results near the shoreline; however, the decrease of nondimensional area density obtained from our experiments was rapid compared to that from the field measurements. Because Goto et al. (2014) derived their regression line using deposits at various inundation distances (0.4–5.4 km), run-up heights (2–10 m), and land slopes without considering the data for no deposits, their analytical method may have overestimated the area density of deposits. Nevertheless, it was uncertain whether the simplification of treating the intricate field topography as a uniform slope was effective. Second, the nondimensional area density proposed in the present study does not consider the effects of topography and waveform. The flow behind the dune was controlled not by the initial wave speed but by the difference in water level in front of and behind the dune (Yoshii et al., 2017). Thus, the shapes of the dune and waveform should be considered in the nondimensional area parameter to improve the accuracy.

To examine further the reproducibility of the spatial distribution obtained in these experiments, it will be important to assemble a database of field data including no-deposit data for various points and tsunamis. Because the thickness of deposits varies considerably in the field, reflecting the local topography (e.g., Nishimura and Miyaji, 1995; Srinivasalu et al., 2009; Goto et al., 2014), a vast amount of field data is needed to reveal the quantitative change of deposits. Considering that flows on flat topography are more subject to local topography (see Section 4.1), deposits on flat topography are more affected by the topography. To acquire sufficient field data, the field investigation reported by (Goto et al., 2014), for example, divided the inundation area into regular grid to collect approximately 1300 readings of tsunami deposit thickness. A systematic survey is preferable not only for efficient collection of the basic information (e.g., thickness and grain size) but also for distributing research points evenly. Such objective data will also help evaluate the variation of tsunami deposit thickness, which can be induced by local topography.

4.4. Flow depth versus sediment thickness (pseudo-concentration)

Because it is relatively easy to measure the flow depth and deposit thickness in the field for contemporary tsunamis, the relationship between these parameters has been used to discuss the sediment transport that takes place during a tsunami. Takashimizu et al. (2012) reported a positive correlation between these parameters (except for in the nearshore region) for deposits on Sendai Plain from the tsunami created by the 2011 Tohoku-oki earthquake. Goto et al. (2014) supported this trend based on a large quantity of field data from Sendai Plain. The regression line obtained by Takashimizu et al. (2012) showed the pseudo-concentration increasing gradually with inundation distance, whereas that obtained by Goto et al. (2014) showed the pseudo-concentration increasing near the inundation limit where the water depth dropped below 0.2 m. Although Goto et al. (2014) found no trend between pseudo-concentration and inundation distance, this probably stemmed from a lack of data for shallow inundation depths.

Because the rapid increase at $L' > 0.9$ in our experiments was derived from a floating load, it was notable that our experiments showed a landward increase of pseudo-concentration as found by the field measurements. This result implied that a floating load occurred in the field. The mechanism of a floating load differs completely from that of a suspended or bed load in not depending on the shear velocity (Yoshii et al., 2017). Thus, we should not treat the deposits caused by a floating load in the same manner as those caused by a suspended or bed load, especially when we infer tsunami parameters from the deposits (see the discussion in Section 4.6).

4.5. Effect of land slope on sediment transport

The increase in concentration was attributed to the bed load. Because the land slope did not affect the suspended sediment in the upper part of the flow, the increase in concentration in the lower part was caused by the bed load (Fig. 9). The time-series of water depth and horizontal velocity for slopes of 0.02 and 0.01 showed little difference where the sediment traps were installed. Thus, the effect of land slope was the most reasonable explanation for the increase in bed load.

The effect of land slope on bed load can be explained from hydraulic and sedimentology perspectives. The hydraulic explanation is that the land slope affected the viscous sublayer and reduced the shear velocity as the land slope increased. Meanwhile, the sedimentology explanation

is that the land slope directly affected the behavior of particles in the bed load, such as rolling, saltation, and sliding. For example, the reflection on the steeper land slope can cause weaker landward saltation. Although the effect of land slope on each contact was small, frequent contacts between the particles and the bed surface could result in a strong effect on the amount of bed load. The speed of the bed load should decrease as the land slope increases in either process; however, the reduced shear velocity should also affect the amount of erosion. Because there was no clear difference due to erosion, particle behavior was the more plausible explanation.

It is a notable characteristic of tsunami inundation that tsunamis flow uphill unlike natural streams of water. This run-up flow necessarily results in a return flow; thus, this characteristic has been indirectly discussed as an effect of the return flows. As reported by Bahlburg and Spiske (2012), the resulting deposits can be affected considerably by the remigration of sediment due to the return flow. Because the return-flow acceleration is controlled by the land slope (Fig. 3), the land slope has a profound influence on the distribution of tsunami deposits by changing the balance between sediment supply due to inundation flow and sediment remigration due to return flow. The importance of land slope was also confirmed by a numerical simulation (Apotsos et al., 2011).

The remarkable difference in bed load on different bed slopes raises fundamental questions as to whether sediment transport on sloping topography is the same as that on a flat floor. It is widely known that land slope influences sediment transport, especially in river flows, because the sediment transport changes from being dominated by suspended-bed load to a debris-flow phase, reflecting the land slope. However, there has been little discussion of sediment transport by uphill flows. For example, for sediment to be transported up a slope, the inundation flow must continue to provide energy to the sediment to compensate for the potential energy that the sediment gains. Furthermore, the land slope can affect the bed load by changing the direction of bouncing during saltation. Because the belief has been that sediment transport during tsunamis is caused mainly by the suspended load because of its high shear velocity, the bed load has been treated as less important. Therefore, the aim of experimental studies has been to validate the role of the suspended load, and that of the bed load has not been investigated (e.g., Takahashi et al., 2000; Yoshii et al., 2009; Takahashi et al., 2011). Experiments with sloping topographies (e.g., Sugawara et al., 2004; Harada et al., 2011) have not measured the sediment transport during the inundation flow, probably because of its small experimental scale.

Based on our results, we should firstly verify the applicability to sloping topography of the conventional bed-load formulae that assume a flat topography. Although it is technically important to examine whether the coefficients in the bed-load formulae remain valid for the stronger flow of a tsunami (Jaffe et al., 2016), we also need to examine whether the coefficients remain valid for different slopes because the coefficients should encompass the effect of bed slope. Because land slope affects the bed load in both the inundation and return flows, it can have a profound effect on the results of numerical simulations. It is unclear whether we can extend the sediment-transport formulae aimed at river flow to sediment transport caused by the tsunami inundation flow. However, these formulae would at least contribute to accurate estimation of sediment transport due to the return flow. It should be noted that the bed slope may change not only the amount of sediment transport but also the sedimentary structures of the deposits.

4.6. Reconstruction of tsunami scale from deposits

The inundation limit has been a simple and reliable index with which to reconstruct the scale of a tsunami. Hence, there is an ongoing and noticeable argument about the difference between the inundation limit and the extent of deposits (e.g., Abe et al., 2012). The inundation limit is essential information for evaluating the scale of a tsunami via numerical simulations because numerical simulations of tsunami inundation are calibrated to fit the observed inundation limit. Therefore, the tsunami scale and the amount of crustal movement estimated by numerical models increase when we assume that the difference is appreciable (e.g., Namegaya and Satake, 2014).

The difference between the flow distance and the inundation limit on nearly flat topography should not be constant because the inundation limit on a nearly flat slope is governed by the water mass, as mentioned above. The inundation limit can reach far inland as the topography becomes flat (Fig. 7 (a)). If there are successive wave incursions, the inundation limit reflects the water mass supplied by the train of waves. Thus, it is difficult to evaluate quantitatively the difference between tsunami inundation and the extent of deposits.

A better way to reconstruct the scale of a tsunami would be to estimate the wave speed from the flow distance (extent of sandy deposits). There are several advantages to using the flow distance instead of the inundation limit. First, it is feasible to identify sandy deposits even in old geological strata obtained by core sampling. Thus, the extent of the sandy deposits should be more-reliable geological information, although geochemical evidence (e.g., Chagué-Goff et al., 2017) and microscopic footprints such as muddy deposits (e.g., Chagué-Goff et al., 2012), diatoms (e.g., Hemphill-Haley, 1996), and DNA (Szczuciński et al., 2016) could be used to trace the inundation limit. Second, the reconstruction method is simple and robust because the flow distance depends only on land slope and the wave speed at the beach (Eq. (5) or (6)). Moreover, offshore wave propagation and transformation are relatively uncomplicated compared with inland inundation; the former two aspects can be calculated using a two-dimensional model.

We should consider the following uncertainties and evaluate the prediction accuracy. One uncertainty arises from the accuracy of the extent of sandy deposits inferred from geological information. According to our results, the thickness of deposits decreased to 0.1% of that at the shoreline. Because the maximum thickness in the field is commonly < 1 m (Peters and Jaffe, 2010a), the thickness decreased to 1 mm or less, which is near the minimum observable thickness. The distribution of deposits can be sparse and subject to weather; thus, the extent of sandy deposits is likely to underestimate the actual flow distance. Another potential cause of uncertainty is the deceleration of the tsunami inundation. Many field surveys of tsunami deposits were conducted on plain fields with slopes < 0.01 (e.g., Shishikura et al., 2007; Sawai et al., 2007; Goto et al., 2014), and numerical studies have been trying to estimate the scale of tsunamis from the inundation or deposition limit (e.g., Namegaya and Satake, 2014). However, the inundation speeds predicted by the models have not been validated properly. The effect of waveform on the inundation speed in the field should be relatively high because the bottom friction in the field is probably smaller than that in experiments. Therefore, we need to clarify the mechanism of the waveform and reflect bottom friction as a possible source of variation.

4.7. Sediment liquefaction

It is premature to draw conclusions about whether tsunamis cause liquefaction. The liquefaction observed in the experiments was not reproducible, which might reflect the considerable variation of wave pressure on the bed. Also, the side wall might influence the water pressure. If the side wall interfered with the experimental setup, the void ratio of the sediment near the side wall might have differed from that of the central sediment. Because most of the liquefied sediment was eroded by the subsequent flow, we could not judge whether this liquefaction occurred only near the wall. Furthermore, the bed condition in the experiments did not follow a similarity rule suitable for geotechnical experiments. Thus, even if this phenomenon was reproducible, it would not mean that tsunamis could cause appreciable liquefaction in the field.

Even though the liquefaction in the experiment was an accidental result, it was noteworthy that liquefied sediment under the erosion showed an undulating deformation that was probably due to the shear stress on the bed. Because the liquefaction caused by an earthquake is universal, it is conceivable that a certain amount of sediment becomes liquefied before the tsunami arrives. In fact, recent field studies have revealed liquefaction underneath tsunami deposits (Martin and Bourgeois, 2012; Goto et al., 2012). If the liquefaction reaches deeper than the erosion, the tsunami may leave discriminative sedimentary structures (e.g., inflection or shearing) on the erosion surface or the deeper stratum. These three-dimensional sedimentary structures would be difficult to observe by core sampling, but might be detected by using ground-penetrating radar. The liquefaction depends on the earthquake shock, and its deformation depends on the scale of the tsunami. Thus, detecting the sedimentary structure associated with both earthquake and tsunami could help to distinguish tsunami deposits from other deposits such as storm-surge deposits.

4.8. Deposition process

Inverse grading has conventionally been attributed to the vertical segregation of particles resulting from collisions among grains in the highly concentrated layer near the bed. The dispersive pressure is believed to maintain the inverse grain segregation in the sediment transport by supplying more upward energy to larger particles (Bagnold, 1954). However, from the grain distribution measured in a previous experiment ($\beta = 0.02$) (Yoshii et al., 2017), we found that inverse grain segregation did not occur in the sediment transport and that the coarse sand should have concentrated near the bed if the sediment settled without shifting. Because the vertical distribution on the gentler slope was similar to that for $\beta = 0.02$, the inversely graded deposits were not due to the vertical size segregation in the sediment transport. The inverse grading did not result from the streamwise size segregation (Hand, 1997) because inverse grading was observed at the substantially eroded part that was the major source of sediment. Thus, there must be mechanisms during the deposition that reverse the vertical distribution of the grain size during the deposition.

Kinetic sieving (Middleton, 1970) is the most reasonable explanation for the formation of the lower inversely graded layer (Fig. 12). This is because smaller particles can fall into the gaps between larger particles even in the very rapid deposition behind the dune. The particles could not move uphill in the rapid deposition (Fig. 12 (b-1)); thus, the thickness of the inversely graded layer was less than that of the bed-load layer, and the larger particles existed at the bed (Fig. 12 (b-2)). Prolonged deposition would promote grain segregation by kinetic sieving by reworking the larger particles in the bed load (Fig. 12 (c-1)). Because the critical shear velocity of larger particles is higher than that of smaller ones and larger particles are less likely to be buried under slow deposition, the larger particles are subject more to the continuing flow. Therefore, the larger particles were lifted and the inversely graded layer thickened as the depositional speed decreased. This depositional process explains why the larger particles appeared on the surface (Fig. 12 (c-2)) even though the $D50$ value showed that the normal grading resulted from the suspended sedimentation (Fig. 8).

The thickness of the inverse grading formed in the rapid deposition should depend on the size of the large particles included in the bed materials. Sumner et al. (2008) used an annular flume to reveal that the sedimentary structure is related to the depositional speed and the forms of inverse grading arise in the slow (prolonged) deposition. The reason that the inverse grading was unclear in the rapid deposition in their experiments might be the insufficient thickness of the inverse grading layer being observed. Considering the narrow grain-size distribution (50–300 μ m) in their experiments, the thickness of the inversely graded layer could have been less than a tenth of our result (< 1 mm). The sandy tsunami deposits in the field are basically well sorted; hence, the inverse grading formed in rapid deposition would be difficult to identify. Therefore, the sedimentary structure of the deposits can be classified as structureless.

In contrast to the inverse grading in the lower subunit, that in the upper subunit should stem partly from the vertical mixing of grains in the sediment transport. Because the strong turbulent flow migrates coarse sediment toward the upper part of the water, it can result in a nearly homogeneous vertical distribution of grain size. This uniform distribution can aggrade coarse particles in the upper part of the deposits, which would look inversely graded or structureless (Fig. 11B).

Although inverse grading is a nearly common sedimentary characteristic of tsunami deposits, it has not been used to infer the hydraulic background. The inverse grading of tsunami deposits is believed to imply a high sediment concentration because inverse grading is attributed to grain collisions in a traction carpet. However, kinetic sieving can be a more common process of inverse grading in tsunami deposits because it can occur even in sediment transport that is not highly dense (relatively weak flow). In fact, our ongoing study is revealing that coarse sand can appear on the surface even in the experiment with smaller waves (C11). Considering that the uplift of coarse particles is correlated with the speed of deposition, the inversely graded layer can determine the duration of the inundation flow, whereas the normally graded layer can determine the flow speed and depth (e.g., Jaffe and Gelfenbuam, 2007; Tang and Weiss, 2015).

Further investigation is needed to develop a method for reconstructing the hydraulic parameters of a tsunami from the inversely graded layer. There are still some major problems that remain to be solved. First, the inverse grading found in the field is not thoroughly confirmed to be made by kinetic sieving. The Shields number

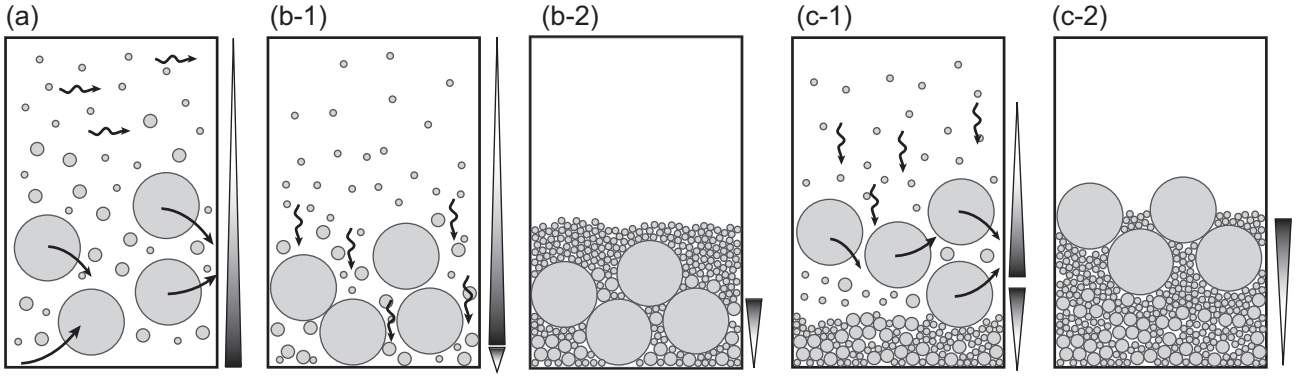

Fig. 12. Schematics of the depositional process of inverse grading: (a) movement of particles in sediment transport; (b-1) infiltration of fine particles into the gaps between large particles (kinetic sieving); (b-2) deposits formed in rapid deposition; (c-1) reworking of large particles in the bed load; (c-2) deposits formed in gradual deposition. The triangles on the right-hand side of each figure indicate the vertical grain-size distribution. The normal and inverted triangles show upward fining and upward coarsening, respectively.

(nondimensional shear velocity) in this experiment (up to 8) is slightly smaller than that in the field (up to 10) and the wave duration can be shorter. A traction carpet potentially occurs in such strong and long flow. Second, the inverse grading layer caused by kinetic sieving in the field can be thinner than that observed in this experiment because the effect depends on the grain-size distribution of the transported materials. Considering the scale ratio of this experiment to the field, the grain size in this experiment is larger than that of fine sand observed in the field. Finer and better-sorted sand will make kinetic sieving less effective. Third, the grain-size distribution, flow speed, and depositional speed can affect the structure of the inversely graded layer. Thus, different hydraulic performances might form similar sedimentary structures. Because kinetic sieving occurs in a deposition process, kinetic sieving is compatible with a traction carpet; hence, the inverse grading can stem from two different processes. Therefore, it is essential to understand the parameter sensitivity to establish a theoretical description of the deposition process.

5. Conclusion

The TSTLE project that involved experiments on land slopes of 0.00–0.02 enabled us to investigate the hydraulic features of tsunami inundation, sedimentary transport, and the sedimentary characteristics of deposits on the alluvial lowland. As the land slope decreased, the bed load increased considerably and carried more coarse sand inland. The fraction of offshore-originated sediments in the inland deposits decreased with land slope, reflecting the stronger inundation flow and weaker return flow. The nondimensional area density and distance showed the potential for generalizing the spatial distribution of sandy deposits for different topographies and incident waves. The inundation limit reached farther inland than the flow distance on the flat topography, reflecting the inland water mass, and formed thin muddy deposits between the inundation limit and the flow distance. Considering that the inundation limit on the nearly flat topography can be affected considerably by a train of waves, the flow distance (i.e., the extent of sandy deposits) was deemed to be a better parameter with which to reconstruct the wave scale. The inverse grading observed in the deposits was attributed to kinetic sieving and was thickened by the bed load. The shearing deformation of liquefied sediments might be evidence of earthquake tsunamis.

The TSTLE project has now completed all its planned experiments. These have supplied multifaceted information regarding wave propagation, flow characteristics, sediment transport, topography change, and the resulting deposits and their sedimentary structures. Our ongoing studies will provide more-specific information about the sedimentary structures of deposits. These experiments fairly simplified the tsunami waves and topography. To link our experimental results with those of field investigations, we need to examine how the complexity of the hydraulic, topographic, and geological features observed in the field affects the sediment transport and the resulting deposits. However, it would be impractical to do so experimentally because the type of large-scale experiment reported herein is extremely time consuming and expensive. Instead, numerical models should be developed to further investigate deposits for different wave forms, number of waves, topographies, and bed materials. Our series of experiments will contribute greatly to the development of numerical simulations as a source of validation and calibration data.

Acknowledgments

We thank Daisuke Inaba, Yoshihiro Tanaka, Yoshinori Goto, and Takayuki Sumita for assisting us with the experimental setup and measurements. We are indebted to Masakazu Watanabe, Rie Fujisawa, and Sachiko Iizuka for their assistance with sampling and laboratory analysis. We also thank Yasutaka Watanabe for helpful discussions about liquefaction. Critical comments on the original manuscript from two anonymous reviewer helped us to improve the paper. The experimental data used in this study are available at https://doi.org/10.17632/7348bmbbsx.1.

Funding

This research did not receive any specific grant from funding agencies in the public, commercial, or not-for-profit sectors.

Conflict of interest

None.

Appendix A. Supplementary data

Supplementary data to this article can be found online at https://doi.org/10.1016/j.margeo.2018.03.007.

References

Abe, T., Goto, K., Sugawara, D., 2012. Relationship between the maximum extent of tsunami sand and the inundation limit of the 2011 Tohoku-oki tsunami on the Sendai Plain, Japan. Sediment. Geol. 282, 142–150.
Apotsos, A., Gelfenbaum, G., Jaffe, B., Watt, S., Peck, B., Buckley, M., Stevens, A., 2011. Tsunami inundation and sediment transport in a sediment-limited embayment on American Samoa. Earth Sci. Rev. 107 (1), 1–11.
Bagnold, R.A., 1954. Experiments on a gravity-free dispersion of large solid spheres in a Newtonian fluid under shear. Proc. R. Soc. Lond. A Math. Phys. Sci. 225 (1160), 49–63.
Bahlburg, H., Spiske, M., 2012. Sedimentology of tsunami inflow and backflow deposits: key differences revealed in a modern example. Sedimentology 59 (3), 1063–1086.
Chagué-Goff, C., Andrew, A., Szczuciński, W., Goff, J., Nishimura, Y., 2012. Geochemical signatures up to the maximum inundation of the 2011 Tohoku-oki tsunami - implications for the 869AD Jogan and other palaeotsunamis. Sediment. Geol. 282, 65–77.
Chagué-Goff, C., Szczuciński, W., Shinozaki, T., 2017. Applications of geochemistry in tsunami research: a review. Earth Sci. Rev. 165, 203–244.
Falvard, S., Paris, R., 2017. X-ray tomography of tsunami deposits: towards a new depositional model of tsunami deposits. Sedimentology 64 (2), 453–477.
Gelfenbaum, G., Jaffe, B., 2003. Erosion and sedimentation from the 17 July, 1998 Papua New Guinea tsunami. Pure Appl. Geophys. 160 (10-11), 1969–1999.
Gelfenbaum, G., Vatvani, D., Jaffe, B., Dekker, F., 2007. Tsunami Inundation and Sediment Transport in Vicinity of Coastal Mangrove Forest. Coastal Sediments '07 - Proceedings of 6th International Symposium on Coastal Engineering and Science of Coastal Sediment Processes.
Goff, J., Nichol, S., Kennedy, D., 2010. Development of a palaeotsunami database for New Zealand. Nat. Hazards 54 (2), 193–208.
Goto, K., Chagué-Goff, C., Fujino, S., Goff, J., Jaffe, B., Nishimura, Y., Richmond, B., Sugawara, D., Szczuciński, W., Tappin, D., Witter, R., Yulianto, E., 2011. New insights of tsunami hazard from the 2011 Tohoku-oki event. Mar. Geol. 290 (1-4), 46–50.
Goto, K., Hashimoto, K., Sugawara, D., Yanagisawa, H., Abe, T., 2014. Spatial thickness variability of the 2011 Tohoku-oki tsunami deposits along the coastline of Sendai Bay. Mar. Geol. 358, 38–48.
Goto, K., Sugawara, D., Abe, T., Haraguchi, T., Fujino, S., 2012. Liquefaction as an important source of the A.D. 2011 Tohoku-oki tsunami deposits at Sendai Plain, Japan. Geology 40 (10), 887–890.
Hand, B.M., 1997. Inverse grading resulting from coarse-sediment transport lag. J. Sediment. Res. 67 (1), 124–129.
Harada, K., Imai, K., Tran, T.A., Fujiki, Y., 2011. Hydraulic experiment on sand deposit by tsunami run-up with land slope. J. JSCE, Ser. B2 (Coast. Eng.) 67 (2), 252–255 (in Japanese with an English abstract).
Hemphill-Haley, E., 1996. Diatoms as an aid in identifying late-holocene tsunami deposits. Holocene 6 (4), 439–448.
International Atomic Energy Agency, 2015. The Fukushima Daiichi Accident. International Atomic Energy Agency, Vienna.
Jaffe, B., Gelfenbuam, G., 2007. A simple model for calculating tsunami flow speed from tsunami deposits. Sediment. Geol. 200 (3), 347–361.
Jaffe, B., Goto, K., Sugawara, D., Gelfenbaum, G., La Selle, S., 2016. Uncertainty in tsunami sediment transport modeling. J. Disaster Res. 11 (4), 647–661.
Johnson, J., Delbecq, K., Kim, W., Mohrig, D., 2016. Experimental tsunami deposits: linking hydrodynamics to sediment entrainment, advection lengths and downstream fining. Geomorphology 253, 478–490.
Kain, C., Gomez, C., Hart, D., Wassmer, P., Goff, J., Starheim, C., 2014. Assessing topographic controls on flow direction in washover deposits using measurements of magnetic fabric. Mar. Geol. 350, 16–26.
Martin, M.E., Bourgeois, J., 2012. Vented sediments and tsunami deposits in the Puget Lowland, Washington differentiating sedimentary processes. Sedimentology 59 (2), 419–444.
Middleton, G.V., 1970. Experimental studies related to problems of flysch sedimentation. In: Flysch Sedimentology in North America. vol. 7. Geological Association of Canada,

pp. 253–272.
Moore, A., McAdoo, B., Ruffman, A., 2007. Landward fining from multiple sources in a sand sheet deposited by the 1929 Grand Banks tsunami, Newfoundland. Sediment. Geol. 200 (3-4), 336–346.
Namegaya, Y., Satake, K., 2014. Reexamination of the A.D. 869 Jogan earthquake size from tsunami deposit distribution, simulated flow depth, and velocity. Geophys. Res. Lett. 41 (7) 2013GL058678.
Nanayama, F., 2008. Sedimentary characteristics and depositional processes of onshore tsunami deposits. An example of sedimentation associated with the 12 July 1993 Hokkaido-Nansei-oki earthquake tsunami. In: Tsunamiites - Features and Implications, pp. 63–80.
Nanayama, F., Satake, K., Furukawa, R., Shimokawa, K., Atwater, B., Shigeno, K., Yamaki, S., 2003. Unusually large earthquakes inferred from tsunami deposits along the Kuril trench. Nature 424 (6949), 660–663.
Naruse, H., Abe, T., 2017. Inverse tsunami flow modeling including nonequilibrium sediment transport, with application to deposits from the 2011 Tohoku-Oki tsunami. J. Geophys. Res. Earth Surf. 122 (11) 2017JF004226.
Naruse, H., Fujino, S., Suphawajruksakul, A., Jarupongsakul, T., 2010. Features and formation processes of multiple deposition layers from the 2004 Indian Ocean Tsunami at Ban Nam Kem, southern Thailand. Island Arc 19 (3), 399–411.
Nishimura, Y., Miyaji, N., 1995. Tsunami deposits from the 1993 Southwest Hokkaido earthquake and the 1640 Hokkaido Komagatake eruption, northern Japan. Pure Appl. Geophys. 144 (3-4), 719–733.
Peters, R., Jaffe, B., 2010a. Database of Recent Tsunami Deposits. U.S. Geological Survey Open-File Report 2010-1172, 12, and database.
Peters, R., Jaffe, B., 2010b. Identification of Tsunami Deposits in the Geologic Record: Developing Criteria Using Recent Tsunami Deposits. U.S. Geological Survey Open-File Report 2010-1239. pp. 39.
Pritchard, D., Dickinson, L., 2008. Modelling the sedimentary signature of long waves on coasts: implications for tsunami reconstruction. Sediment. Geol. 206 (1), 42–57.
Satake, K., Namegaya, Y., Yamaki, S., 2008. Numerical simulation of the AD 869 Jogan tsunami in Ishinomaki and Sendai plains. Annu. Rep. Active Fault Paleoearthq. Res. 8, 71–89 (in Japanese with an English abstract).
Sawai, Y., Namegaya, Y., Okamura, Y., Satake, K., Shishikura, M., 2012. Challenges of anticipating the 2011 Tohoku earthquake and tsunami using coastal geology. Geophys. Res. Lett. 39 (21), L21309.
Sawai, Y., Shishikura, M., Okamura, Y., Takada, K., Matsu'ura, T., Aung, T.T., Kmataki, T., Sato, N., 2007. A study of paleotsunami using handy geoslicer in Sendai Plain (Sendai, Natori, Iwanuma, Watari, and Yamamoto), Miyagi, Japan. Annu. Rep. Active Fault Paleoearthq. Res. 7, 47–80 (in Japanese with an English abstract).
Shi, S., Dawson, A., Smith, D., 1995. Coastal sedimentation associated with the December 12th, 1992 tsunami in Flores, Indonesia. Pure Appl. Geophys. 144 (3-4), 525–536.
Shishikura, M., Sawai, Y., Okamura, Y., Komatsubara, J., Aung, T.T., Ishiyama, T., Fujiwara, O., Fujino, S., 2007. Age and distribution of tsunami deposit in the Ishinomaki Plain, Northeastern Japan. Annu. Rep. Active Fault Paleoearthq. Res. (7), 31–46 (in Japanese with an English abstract).
Smith, D., Foster, I., Long, D., Shi, S., 2007. Reconstructing the pattern and depth of flow onshore in a palaeotsunami from associated deposits. Sediment. Geol. 200 (3-4), 362–371.
Soulsby, R., Smith, D., Ruffman, A., 2007. Reconstructing Tsunami Run-up From Sedimentary Characteristics - A Simple Mathematical Model. 6th International Symposium on Coastal Engineering and Science of Coastal Sediment Process. pp. 1075–1088.
Spiske, M., Piepenbreier, J., Benavente, C., Kunz, A., Bahlburg, H., Steffahn, J., 2013. Historical tsunami deposits in Peru: sedimentology, inverse modeling and optically stimulated luminescence dating. Quat. Int. 305, 31–44.
Srinivasalu, S., Rao, N.R., Thangadurai, N., Jonathan, M.P., Roy, P.D., Mohan, V.R., Saravanan, P., 2009. Characteristics of 2004 tsunami deposits of the northern Tamil Nadu coast, southeastern India. Bol. Soc. Geol. Mex. 61 (1), 111–118.
Sugawara, D., Goto, K., 2012. Numerical modeling of the 2011 Tohoku-oki tsunami in the offshore and onshore of Sendai Plain, Japan. Sediment. Geol. 282, 110–123.
Sugawara, D., Minoura, K., Imamura, F., Hirota, T., Sugawara, M., Ohkubo, S., 2004. Hydraulic experiments regarding tsunami sedimentation. Mem. Geol. Soc. Jpn. (58), 153–162.
Sumner, E., Amy, L., Talling, P., 2008. Deposit structure and processes of sand deposition from decelerating sediment suspensions. J. Sediment. Res. 78 (8), 529–547.
Szczuciński, W., Kokociński, M., Rzeszewski, M., Chagué-Goff, C., Cachão, M., Goto, K., Sugawara, D., 2012. Sediment sources and sedimentation processes of 2011 Tohoku-oki tsunami deposits on the Sendai Plain, Japan - insights from diatoms, nannoliths and grain size distribution. Sediment. Geol. 282, 40–56.
Szczuciński, W., Pawłowska, J., Lejzerowicz, F., Nishimura, Y., Kokociński, M., Majewski, W., Nakamura, Y., Pawlowski, J., 2016. Ancient sedimentary DNA reveals past tsunami deposits. Mar. Geol. 381, 29–33.
Takahashi, T., Kurokawa, T., Fujita, M., Shimada, H., 2011. Hydraulic experiment on sediment transport due to tsunamis with various sand grain size. J. Jpn. Soc. Civil Eng. Ser. B2 (Coast. Eng.) 67 (2), I_231–I_235 (in Japanese with an English abstract).
Takahashi, T., Shuto, N., Imamura, F., Asai, D., 2000. Modeling sediment transport due to tsunamis with exchange rate between bed load layer and suspended load layer. In: Proceedings of the International Conference on Coastal Engineering. vol. 276. pp. 1508–1519.
Takashimizu, Y., Urabe, A., Suzuki, K., Sato, Y., 2012. Deposition by the 2011 Tohoku-oki tsunami on coastal lowland controlled by beach ridges near Sendai, Japan. Sediment. Geol. 282, 124–141.
Tang, H., Wang, J., Weiss, R., Xiao, H., 2018. TSUFLIND-EnKF: inversion of tsunami flow depth and flow speed from deposits with quantified uncertainties. Mar. Geol. 396 (1), 16–25.
Tang, H., Weiss, R., 2015. A model for tsunami flow inversion from deposits (TSUFLIND). Mar. Geol. 370, 55–62.
Wang, J.-X., Tang, H., Xiao, H., Weiss, R., 2018. Inferring tsunami flow depth and flow speed from sediment deposits based on Ensemble Kalman filtering. Geophys. J. Int. 212 (1), 646–658.
Witter, R., Jaffe, B., Zhang, Y., Priest, G., 2012. Reconstructing hydrodynamic flow parameters of the 1700 tsunami at Cannon Beach, Oregon, USA. Nat. Hazards 63 (1), 223–240.
Yamaguchi, N., Sekiguchi, T., 2015. Effects of tsunami magnitude and terrestrial topography on sedimentary processes and distribution of tsunami deposits in flume experiments. Sediment. Geol. 328, 115–121.
Yoshii, T., Ikeno, M., Matsuyama, M., 2009. Experimental Study of Sediment Transport Caused by Tsunami. Proceedings of Coastal Dynamics 2009. pp. 1–11.
Yoshii, T., Tanaka, S., Matsuyama, M., 2017. Tsunami deposits in a super-large wave flume. Mar. Geol. 391, 98–107.

Supplementary Information

Tsunami inundation, sediment transport, and deposition process of tsunami deposits on coastal lowland inferred from the Tsunami Sand Transport Laboratory Experiment (TSTLE)

Yoshii, T., Tanaka, S., and Matsuyama, M.

A paper in "Marine Geology"

Supplementary information A. Supplementary figures

This section supplies figures showing the hydraulic parameters (Fig. A.1) and the spatial distributions of topography, deposit, grain size, and chemical content (Fig. A.2).

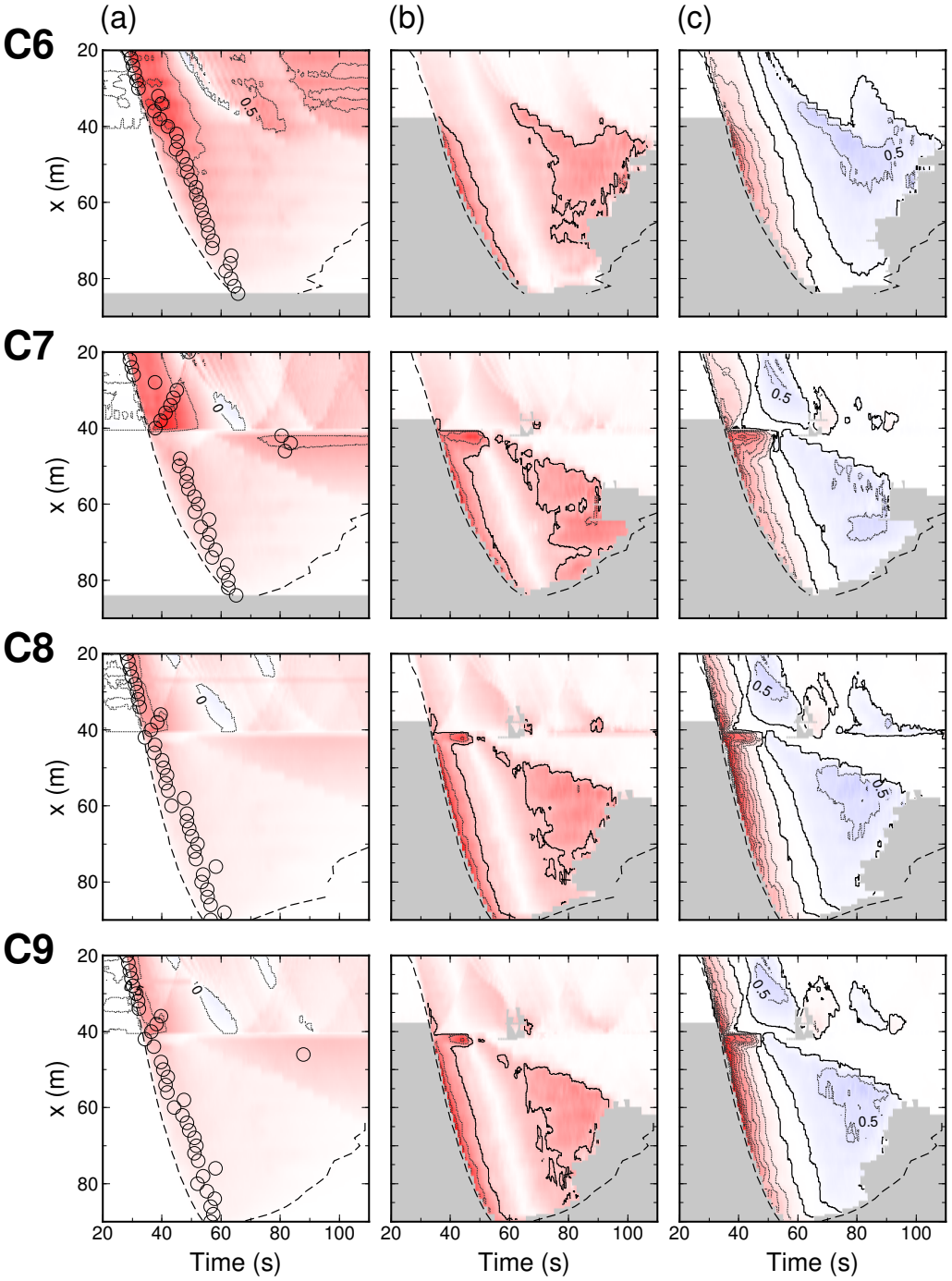

Figure A.1: Time variation of (a) ratio of water level (offshore) and depth (onshore) to maximum water depths at x = 0.5 m, (b) Froude number, and (c) Shields number observed in fixed-bed channel. The broken lines show the position of the wavefront. The black line in the (b) figures shows where the Froude number is 1.0. In the (c) figures, the red and blue shading indicates the landward and seaward currents, respectively, and the black bold lines indicate the critical Shields number. The gray areas indicate where no horizontal velocity data were obtained.

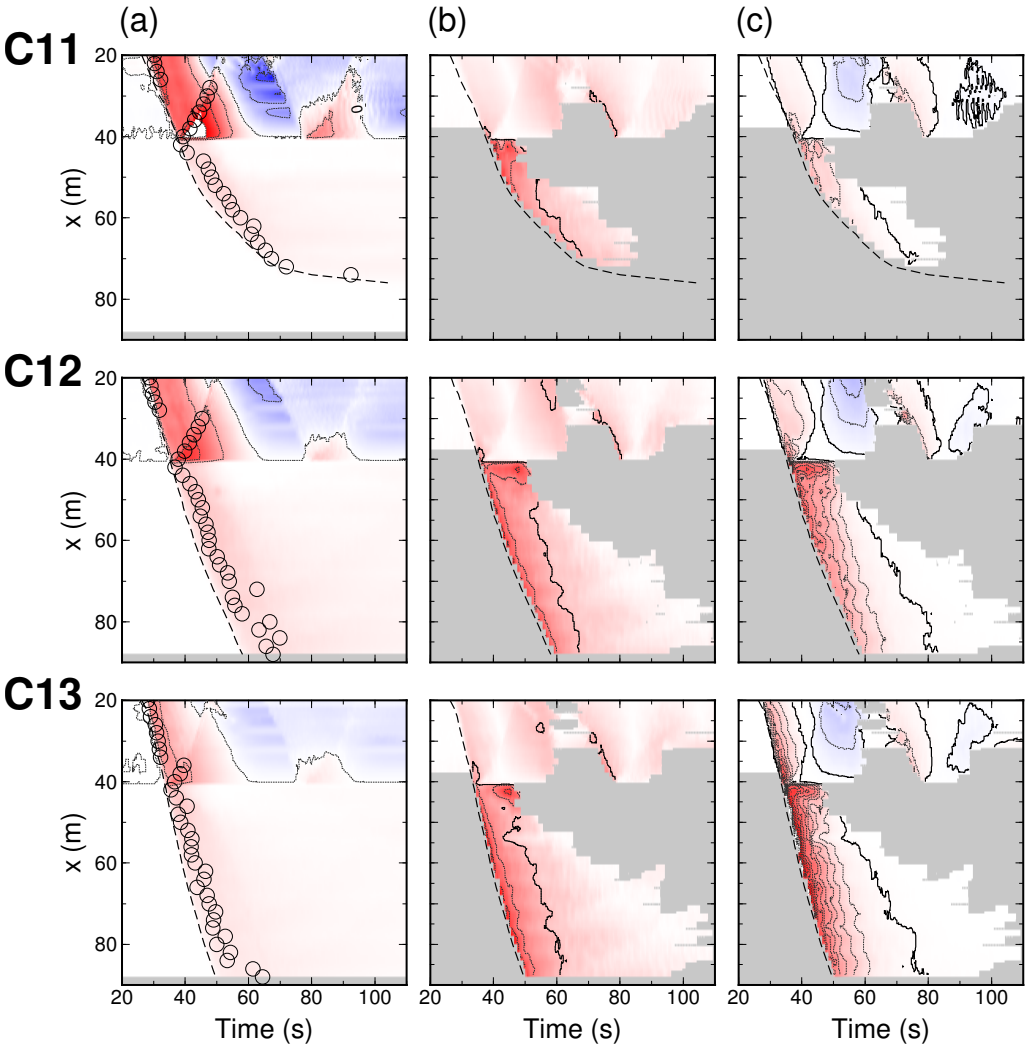

Figure A.1: (Continued)

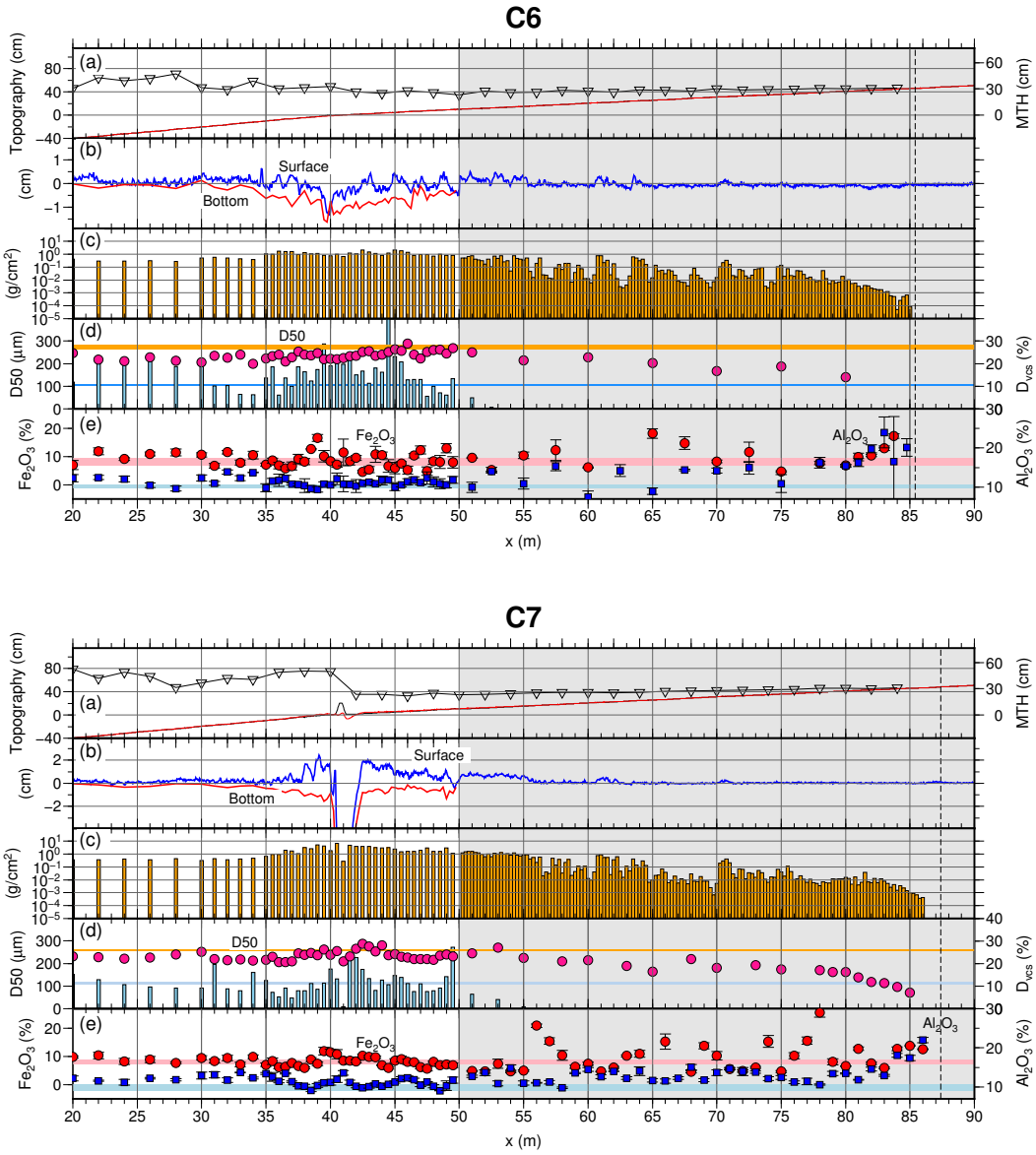

Figure A.2: (a) Topography and maximum tsunami height (MTH) , (b) erosion and topography change, (c) amount of deposit, (d) grain size of deposit, and (e) Fe and Al content in deposit. In (a), the black line shows the pre-experiment topography and the red line shows the post-experiment topography. In (d), the circles and vertical bars show D50 and D_{vcs}, respectively. In (e), the circles and squares indicate the Fe_2O_3 and Al_2O_3 contents, respectively. The error bars for the chemical composition indicate the standard error. The horizontal bars in (d) and (e) indicate the value of the pre-experimental bed (average ± SE). The vertical broken lines indicate the inundation limit. The amount of overflowed sediment, grain size, and chemical composition are shown at x = 91 m on the right-hand vertical axes of (c), (d), and (e).

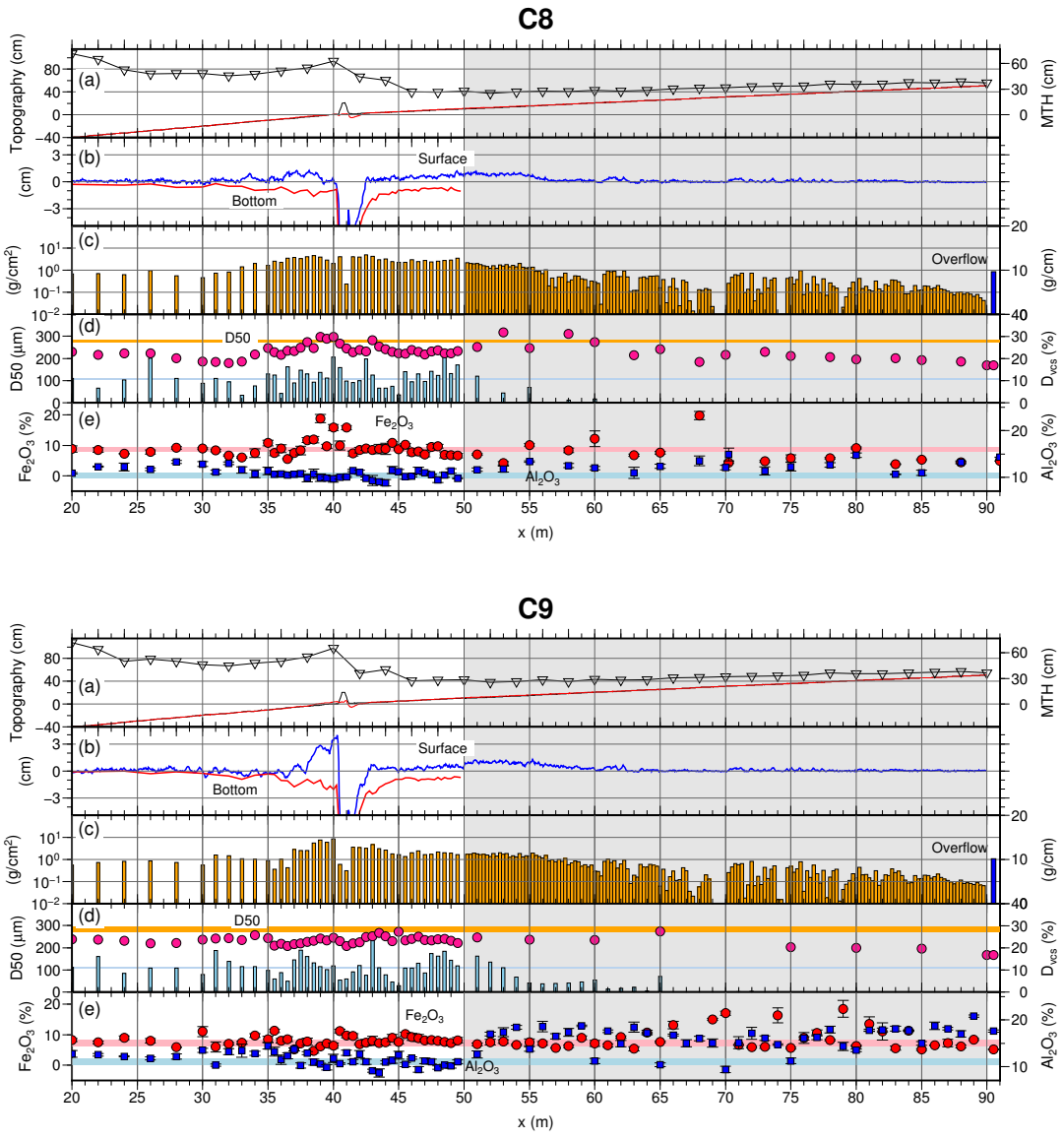

Figure A.2: (Continued)

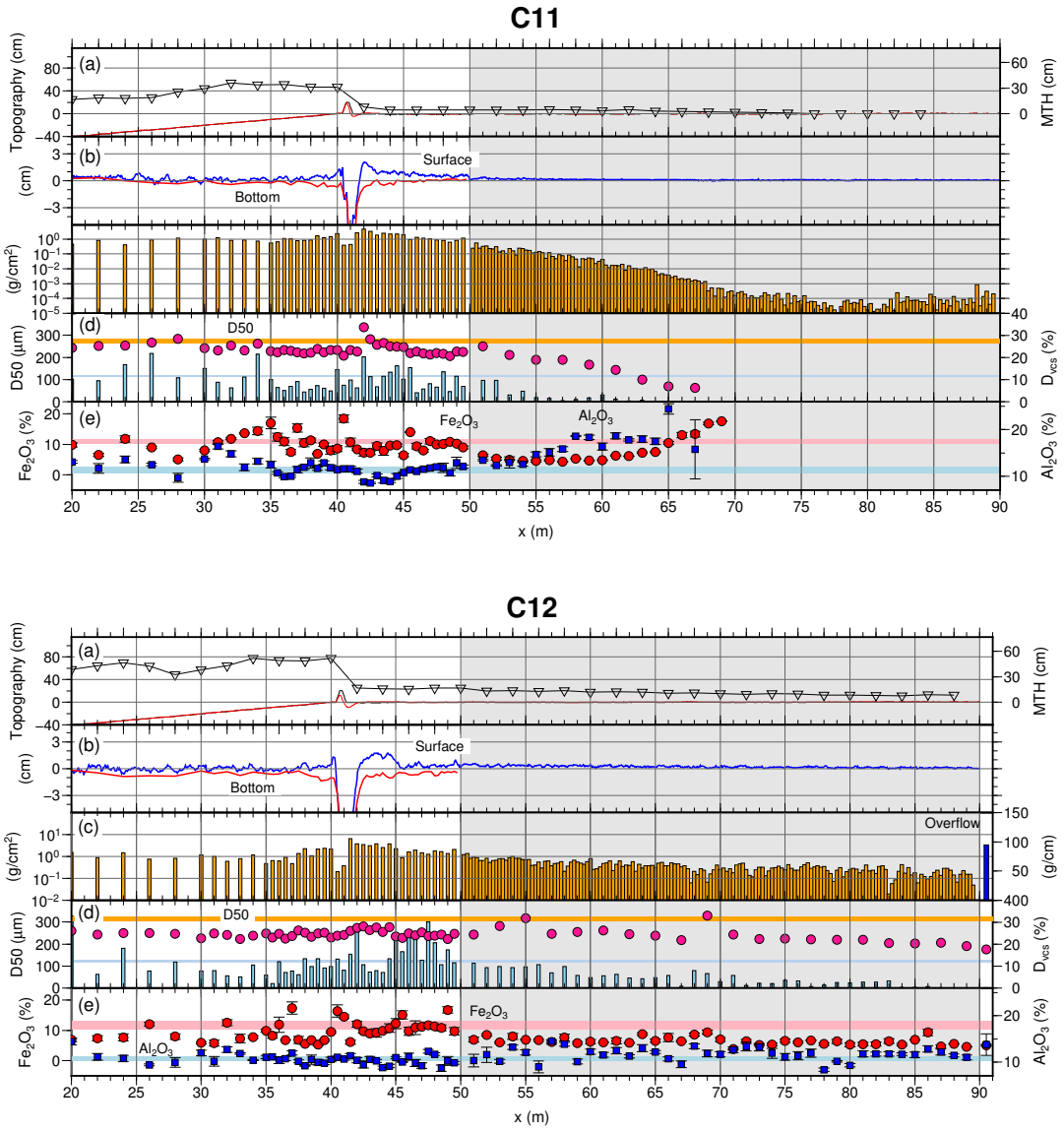

Figure A.2: (Continued)

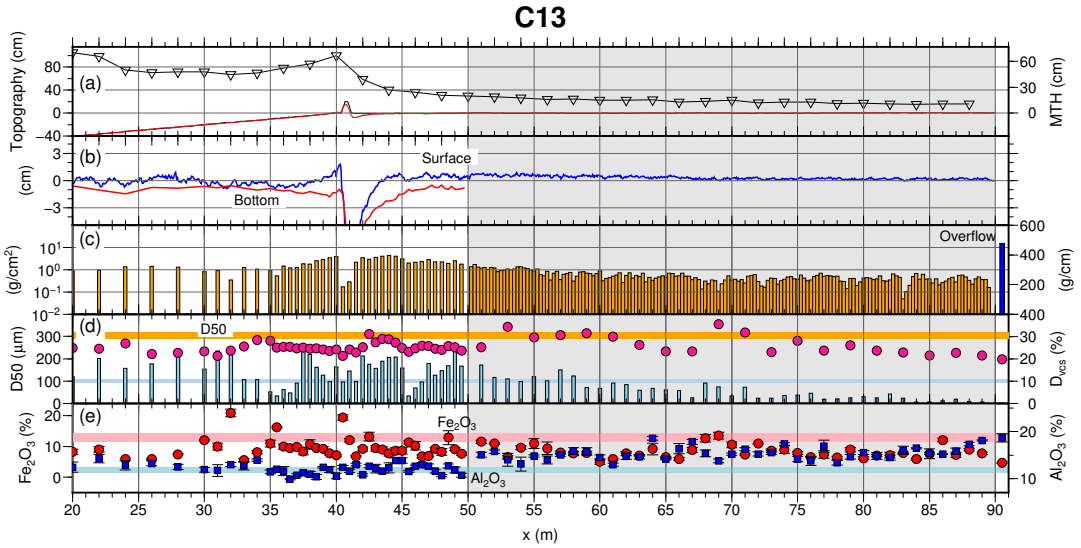

Figure A.2: (Continued)